Superspace Description, Crystal Structures, and Electric Conductivity of the $Ba_4In_{6-x}Mg_xO_{13-x/2}$ Solid Solutions

Artem M. Abakumov,*[,†] Marta D. Rossell,[‡,||] Olga Yu. Gutnikova,[†] Oleg A. Drozhzhin,[†,§] Ludmila S. Leonova,[§] Yuri A. Dobrovolsky,[§] Sergey Ya. Istomin,[†] Gustaaf Van Tendeloo,[‡] and Evgeny V. Antipov[†]

Department of Chemistry, Moscow State University, 119991 Moscow, Russia, EMAT, University of Antwerp, Groenenborgerlaan 171, B-2020Antwerp, Belgium, Institute of Problems of Chemical Physics, Russian Academy of Sciences, Acad. Semenov av. 1, 142432 Chernogolovka, Moscow Region, Russia, National Center for Electron Microscopy, Lawrence Berkeley National Laboratory, University of California, 1 Cyclotron Road, Berkeley, California 94720

Received February 11, 2008. Revised Manuscript Received April 13, 2008

$Ba_4In_{6-x}Mg_xO_{13-x/2}$ solid solutions have been prepared for $0 \le x \le 0.4$ and their crystal structures have been studied by transmission electron microscopy and X-ray powder diffraction. The compounds adopt a modulated structure with a face-centered orthorhombic average unit cell with $a_0 \approx a_p\sqrt{2}$, $b_0 \approx 20.5$Å, $c_0 \approx a_p\sqrt{2}$ (a_p − parameter of the perovskite subcell) and modulation vector $\mathbf{q} = \alpha\mathbf{a}_0^*$, which is compositionally dependent according to the $Ba_4In_{4+4\alpha}Mg_{2-4\alpha}O_{12+2\alpha}$ formula. The superspace group $Xmm2(\alpha 00)0s0$ with centering vectors (0,1/2,1/2,1/2), (1/2,0,1/2,0), (1/2,1/2,0,1/2) was proposed from electron diffraction and structural considerations. A unified superspace model is constructed to describe the atomic arrangements and the variable oxygen content in the modulated $(In, Mg)_2O_{2+\alpha}$ layers with rock-salt type structure. This model was used to refine the crystal structures of two $x = 0$ ($R_I = 0.040$, $R_P = 0.042$) and $x = 0.4$ ($R_I = 0.062$, $R_P = 0.040$) limiting points of the solid solutions. The cations in these layers adopt a five-fold coordination that can be virtually classified as strongly distorted trigonal bipyramids and tetragonal pyramids. The close similarity of the structural organization of the $Ba_4In_{6-x}Mg_xO_{13-x/2}$ solid solutions, $Sr_4Fe_6O_{13}$ and its anion-deficient derivatives is discussed. Electric conductivity of the $Ba_4In_{6-x}Mg_xO_{13-x/2}$ was studied by impedance spectroscopy indicating mixed ionic-electronic type of conductivity. Electronic conductivity at different $P(O_2)$ was compared for $Ba_4In_6O_{13}$ and $Ba_2In_2O_5$ and discussed taking into account the peculiarities of their crystal structures.

1. Introduction

The $Sr_4Fe_6O_{13}$ perovskite-type oxide (Figure 1) and its anion-deficient derivatives have been a subject of particular attention on account of their potential application as mixed ionic/electronic conductors [1–4] and complex mechanism of anion non-stoichiometry through compositional and displacement modulations in the double NaCl-like $Fe_2O_{2+\alpha}$ layers. The relationship between the modulation parameters, the structure of the $Fe_2O_{2+\alpha}$ iron−oxygen layers, and the oxygen content was initially derived from transmission electron microscopy data;[5–7] it was later investigated using single-crystal diffraction experiments for $Sr_4Fe_6O_{12.92}$[8] and for the closely related $Fe_2(Bi_{0.69}Sr_{2.31})Fe_2O_{9.5-1/2\delta}$.[9] The latter also contains a double iron−oxygen layer alternating with two octahedral perovskite layers instead of one single perovskite layer as in $Sr_4Fe_6O_{12.92}$. Up to now, only a few representatives of this family with modulated structures are found (including the compounds with a complete substitution of Fe by Co+Ga[10] and a partial substitution of Sr by Pb[11]). One can expect that the underlying building principles will be valid for other complex oxides with cations possessing crystal chemistry properties similar to those of the Fe^{3+} cations. The In^{3+} cation in oxide structures often adopts the same coordination numbers from 4 to 6 as Fe^{3+}. For both cations, the brownmillerites $A_2B_2O_5$ are known,[12,13] but In requires

* Corresponding author. E-mail: abakumov@icr.chem.msu.ru. Tel: 7 (495) 939-52-44. Fax: 7 (495) 939-47-88.
† Moscow State University.
‡ University of Antwerp.
|| Lawrence Berkeley National Laboratory.
§ Russian Academy of Sciences.

(1) Avdeev, M.Y.; Patrakeev, M.V.; Kharton, V.V.; Frade, J.R. *J. Solid State Electrochem.* **2002**, *6*, 217–224.
(2) Patrakeev, M.V.; Mitberg, E.B.; Leonidov, I.A.; Kozhevnikov, V.L. *Solid State Ionics* **2001**, *139*, 325–330.
(3) Fisher, C.A.J.; Saiful Islam, M. *J. Mater. Chem.* **2005**, *15*, 3200–3207.
(4) Patrakeev, M.V.; Leonidov, I.A.; Kozhevnikov, V.L.; Kharton, V.V. *Solid State Sciences* **2004**, *6*, 907–913.
(5) Rossell, M.D.; Abakumov, A.M.; Van Tendeloo, G.; Pardo, J.A.; Santiso, J. *Chem. Mater.* **2004**, *16*, 2578–2584.
(6) Rossell, M.D.; Abakumov, A.M.; Van Tendeloo, G.; Lomakov, M.V.; Istomin, S.Ya.; Antipov, E.V. *Chem. Mater.* **2005**, *17*, 4717–4726.
(7) Mellenne, B.; Retoux, R.; Lepoittevin, C.; Hervieu, M.; Raveau, B. *Chem. Mater.* **2004**, *16*, 5006–5013.
(8) Pérez, O.; Mellenne, B.; Retoux, R.; Raveau, B.; Hervieu, M. *Solid State Sci.* **2006**, *8*, 431–443.
(9) Grebille, D.; Lepoittevin, C.; Malo, S.; Pérez, O.; Nguyen, N.; Hervieu, M. *J. Solid State Chem.* **2006**, *179*, 3849–3859.
(10) Pelloquin, D.; Hébert, S.; Pérez, O.; Pralong, V.; Nguyen, N.; Maignan, A. *J. Solid State Chem.* **2005**, *178*, 792–799.
(11) Lepoittevin, C.; Malo, S.; Pérez, O.; Nguyen, N.; Maignan, A.; Hervieu, M. *Solid State Sci.* **2006**, *8*, 1294–1301.
(12) Berastegui, P.; Hull, S.; García-García, F.J.; Eriksson, S.-G. *J. Solid State Chem.* **2002**, *164*, 119–130.
(13) Schmidt, M.; Campbell, S.J. *J. Solid State Chem.* **2001**, *156*, 292–304.

10.1021/cm8004216 CCC: $40.75
Published on Web 06/18/2008

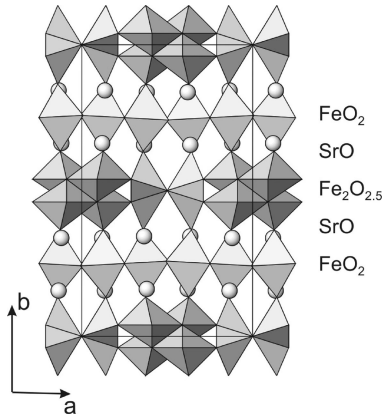

Figure 1. $Sr_4Fe_6O_{13}$ crystal structure. The Fe atoms are in the shaded polyhedra, the Sr atoms are shown as spheres.

a larger A-cation (Ba^{2+}) in comparison with Sr^{2+} for iron to stabilize this structure. Indeed, $Sr_4Fe_6O_{13}$ also has its In-based analogue $Ba_4In_6O_{13}$, which was first synthesized by Kanamaru et al.[14] Its crystal structure was solved by Yoshiasa et al.[15] In contrast to the Fe-based compounds, the oxygen content in $Ba_4In_6O_{13}$ is less sensitive to temperature and partial oxygen pressure and can be changed by heterovalent substitution, which allows the isolation of single phases with required oxygen content.

In this contribution, we describe the preparation of the $Ba_4In_{6-x}Mg_xO_{13-x/2}$ solid solutions and the investigation of their modulated structures by means of transmission electron microscopy and X-ray powder diffraction. We also propose a unified superspace description of the $A_4B_6O_{12+2\alpha}$ compounds (in the sense of ref [16]), which allows us to establish the main structural features from a known modulation vector and provides an initial model for structure refinement from powder diffraction data.

2. Experimental Section

2.1. Synthesis. $Ba_4In_{6-x}O_{13-1.5x}$ samples with $0 \le x \le 0.15$ ($\Delta x = 0.05$) and $Ba_4In_{5.85-x}Mg_xO_{12.775-x/2}$ samples with $0.1 \le x \le 0.4$ ($\Delta x = 0.1$) were prepared from stoichiometric mixtures of $BaCO_3$, In_2O_3, and MgO ("Reakhim", pure for analysis grade). The required amounts of the initial reagents were ground in an agate mortar under acetone, pressed into pellets, and annealed in alumina crucibles in air at 1000°C for 30 h, followed by regrinding and further firing at 1200 °C for 48 h.

2.2. X-ray Powder Diffraction. X-ray powder diffraction (XRD) data were collected on a Huber G670 Guinier diffractometer ($CuK_{\alpha 1}$ radiation, curved Ge monochromator, transmission mode, image plate) with Ge ($a = 5.6576$Å) as an internal standard. X-ray powder diffraction data for crystal structure refinement were collected on a STADI-P diffractometer ($CuK_{\alpha 1}$ radiation, curved Ge monochromator, transmission mode, linear PSD). The JANA2000 program package was used for the Rietveld refinement.[17]

2.3. Transmission Electron Microscopy. Electron diffraction (ED) studies were performed using a Philips CM20 microscope and high-resolution electron microscopy (HREM) was done using a JEOL 4000EX microscope. Energy-dispersive X-ray (EDX) spectra were obtained on the Phillips CM20 with an Oxford INCA system. The HREM images were simulated using the MacTempas software.

2.4. Electric Impedance Spectroscopy. The electric impedance spectroscopy (EIS) measurements were performed using a frequency response analyzer Z-350M (Elins) in the frequency range 1 Hz to 1 MHz, in the temperature range 400−900 °C. The quantitative values of the equivalent circuit components were derived using ZView-2 software.[18] For the EIS measurements, the powder samples of $Ba_4In_6O_{13}$ and $Ba_4In_{6-x}Mg_xO_{13-0.5x}$ were pressed into pellets of 6 mm diameter and calcinated at 1200 °C. Final thicknesses of the $Ba_4In_6O_{13}$ pellets were of 0.8 and 1.8 mm and the thicknesses of the $Ba_4In_{6-x}Mg_xO_{13-0.5x}$ pellets varied in the range of 0.23−0.31 mm. The electrodes were made by printing Pt paste (Heraeus) on the both sides of the pellets followed by firing at 900°C.

3. Results

3.1. Preparation and Preliminary Characterization. $Ba_4In_6O_{13}$ was obtained with a noticeable amount (~5%) of $BaIn_2O_4$ admixture using a high-temperature solid-state reaction starting from the stoichiometric sample composition. Rising the annealing temperature or the time with several intermediate regrindings does not eliminate this admixture phase. The formation of the $BaIn_2O_4$ admixture reflects that either the samples are Ba-depleted or the target compound contains a lower amount of In in comparison with the stoichiometric $Ba_4In_6O_{13}$ composition. To obtain a single-phase compound, we prepared In-deficient samples with nominal composition $Ba_4In_{6-x}O_{13-1.5x}$, $0 \leqslant x \leqslant 0.15$ ($\Delta x = 0.05$). For the $x = 0.15$ composition, a single-phase sample was obtained at the synthesis conditions described in the Experimental Section.

However, EDX analysis on the $Ba_4In_{5.85}O_{12.775}$ sample revealed the ideal Ba:In = 2.00(4):3.00(4) composition. The discrepancy between the EDX results and the bulk composition of the $Ba_4In_{6-x}O_{13-1.5x}$ samples can occur because of the relatively high volatility of barium oxide at high temperatures. Another possibility is an incomplete solid state reaction leaving the $Ba_2In_2O_5$ and $BaIn_2O_4$ admixtures. $Ba_2In_2O_5$ has a perovskite-based structure and can form thin lamellae inside the $Ba_4In_6O_{13}$ phase being invisible on the XRD pattern that was confirmed by the HREM observations (see below). Most probably both Ba volatilization and formation of the thin $Ba_2In_2O_5$ slabs take place resulting in an apparent lack of In in the target sample. This behavior of the $Ba_4In_{6-x}O_{13-1.5x}$ samples was taken into account for the preparation of the $Ba_4In_{6-x}Mg_xO_{13-x/2}$ solid solutions. In-deficient initial compositions resulted in single-phase samples with $x = 0.1$, 0.2, 0.3. In the $x = 0.4$ sample, traces of $Ba_2In_2O_5$ were detected, indicating the limit of the homogeneity range. EDX analysis of the $x = 0.4$ sample provided a $Ba_{3.9(1)}In_{5.7(1)}Mg_{0.4(1)}$ composition, in agreement with the proposed $Ba_4In_{5.6}Mg_{0.4}O_{12.8}$ one.

The formation of solid solutions is confirmed by a monotonic variation of the unit cell parameters with x (Table

(14) Kanamaru, F.; Koizumi, M. *J. Am.Ceram.Soc.* **1973**, *56*, 399–400.
(15) Yoshiasa, A.; Takeno, S.; Iishi, K. *Miner. J.* **1992**, *16*, 40–48.
(16) Perez-Mato, J. M.; Zakhour-Nakhl, M.; Weill, F.; Darriet, J. J. *Mater. Chem.* **1999**, *9*, 2795–2808.
(17) Petricek, V.; Dusek, M. *The Crystallographic Computing System JANA2000*:; Institute of Physics: Praha, Czech Republic, 2000.
(18) *ZView2 for Windows*, version 2.0; Scribner: Charlottesville, VA, 2000.

Table 1. Lattice Parameters for the $Ba_4In_{6-x}Mg_xO_{13-x/2}$ Solid Solutions

x	a_0 (Å)	b_0 (Å)	c_0 (Å)	V (Å^3)
0	5.9394(8)	20.586(2)	5.9600(8)	728.7(1)
0.1	5.9337(6)	20.545(2)	5.9668(5)	727.40(8)
0.2	5.9328(8)	20.511(3)	5.9695(7)	726.4(1)
0.3	5.9316(9)	20.497(3)	5.9717(8)	726.0(1)
0.4	5.9312(9)	20.464(3)	5.9732(8)	725.0(1)

1). The orthorhombic unit cell of $Ba_4In_6O_{13}$ is related to that of perovskite as $a \approx 2a_p\sqrt{2}$, $b \approx 20.6$Å, $c \approx a_p\sqrt{2}$ (a_p is a parameter of the perovskite subcell). However, we have performed the indexation of the XRD powder patterns with a $a_0 = 1/2a$, $b_0 = b$, $c_0 = c$ subcell. The superlattice reflections corresponding to an increased periodicity along the a axis adopt incommensurate positions that vary with the Mg and O content. This will be further shown explicitly using the ED observations. The b_0 parameter and unit-cell volume decrease concomitantly with increasing Mg content, in agreement with the smaller size of the Mg^{2+} cations ($r =$ 0.72 Å, CN = 6) compared to that of the In^{3+} cations ($r =$ 0.79Å, CN = 6). The a_0 and c_0 parameters vary in opposite directions, demonstrating an increase of the orthorhombic distortion with increasing x.

3.2. Electron Diffraction. The ED patterns of the $x = 0$ phase taken along the most prominent zone axes are shown in Figure 2. The reciprocal lattice of the $Ba_4In_{6-x}Mg_xO_{13-x/2}$ solid solutions can be interpreted using a (3+1)D approach. The positions of the spots are given by diffraction vectors $\mathbf{g} = h\mathbf{a}_0^* + k\mathbf{b}_0^* + l\mathbf{c}_0^* + m\mathbf{q}$, $\mathbf{q} = \alpha\mathbf{a}_0^*$; the spots then can be indexed with four $hklm$ indexes. The $hkl0$ reflections

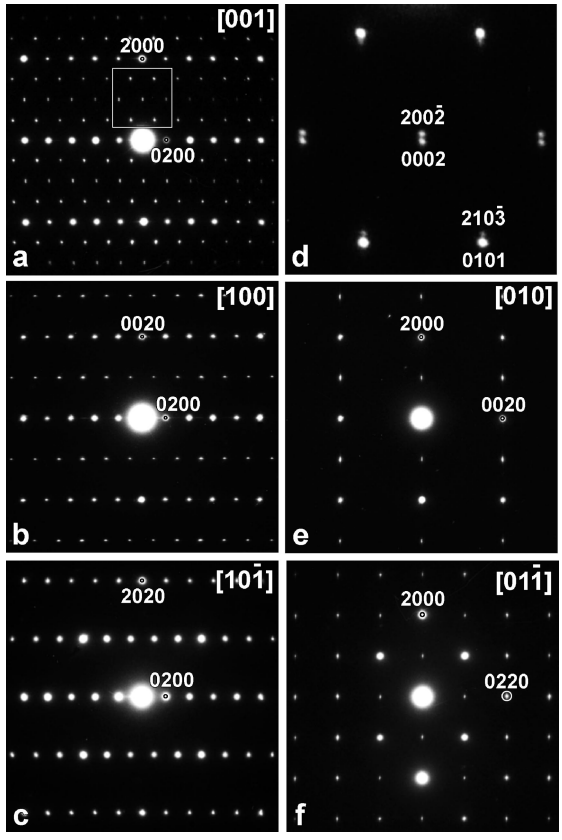

Figure 2. ED patterns of the $x = 0$ compound. (d) represents an enlarged part outlined in (a).

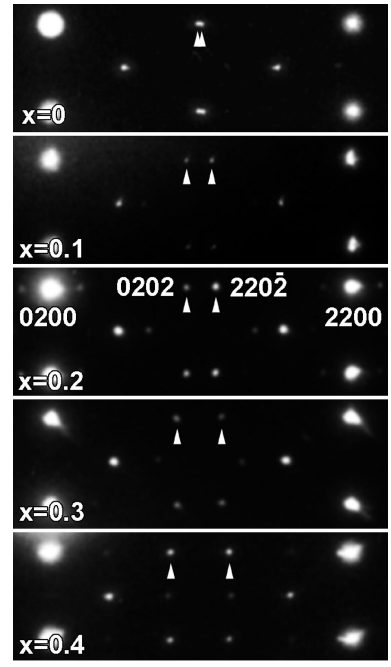

Figure 3. Enlarged parts of the [001] ED patterns of the $Ba_4In_{6-x}Mg_xO_{13-x/2}$ solid solutions with different x values demonstrating a variation of the α value with composition. The satellites are marked with arrowheads.

correspond to the average unit cell, which is face-centered orthorhombic with $a_0 \approx a_p\sqrt{2}$, $b_0 \approx 20.6$Å, $c_0 \approx a_p\sqrt{2}$, i.e., with the lattice parameters from the $x = 0$ row of Table 1. The reflections with $m \neq 0$ are satellites. There is a remarkable difference between the reflection positions on the experimental diffraction patterns and those expected for the $Ba_4In_6O_{13}$ compound with $a = 2a_0$, $b = b_0$, $c = c_0$ and $Iba2$ space group as described in ref 15, which corresponds to the commensurate case with $\alpha = 1/2$. The satellite reflections on the [001], [010], and [01$\bar{1}$] ED patterns do not coincide being separated along **a***. The separation between the satellites becomes prominent on a magnified part of the [001] ED pattern shown in Figure 2d. It indicates an incommensurability with an α component slightly smaller than 1/2. The spots at the $0kl0$, k, $l =$ odd positions are present on the [100] ED pattern (Figure 2b). These reflections seem to violate the extinction conditions imposed by the face-centered unit cell of the average structure. However, the $0kl0$, k, $l =$ odd forbidden spots on the [100] ED pattern actually are the second-order satellites positioned just above and below this reciprocal lattice plane (for example, the 112 and 111 satellites for the 0110 spot). For the commensurate $\alpha = 1/2$ case, the positions of these satellites coincide, but if α does not significantly deviate from 1/2, the relrods of these satellites can intersect the Ewald sphere producing intensity at the $0kl0$, k, $l =$ odd positions.

The ED patterns of the $Ba_4In_{6-x}Mg_xO_{13-x/2}$ solid solutions provide a direct confirmation of the relationship between the oxygen content and the α value. The α value decreases concomitantly with decreasing oxygen content, as it can be seen in Figure 3 by the increased distance between the satellite reflections. For $Ba_4In_{5.6}Mg_{0.4}O_{12.8}$, α reaches its commensurate value of 2/5, which agrees with the 12+2α relationship between the oxygen content and the length of the modulation vector. Thus the general formula of the solid

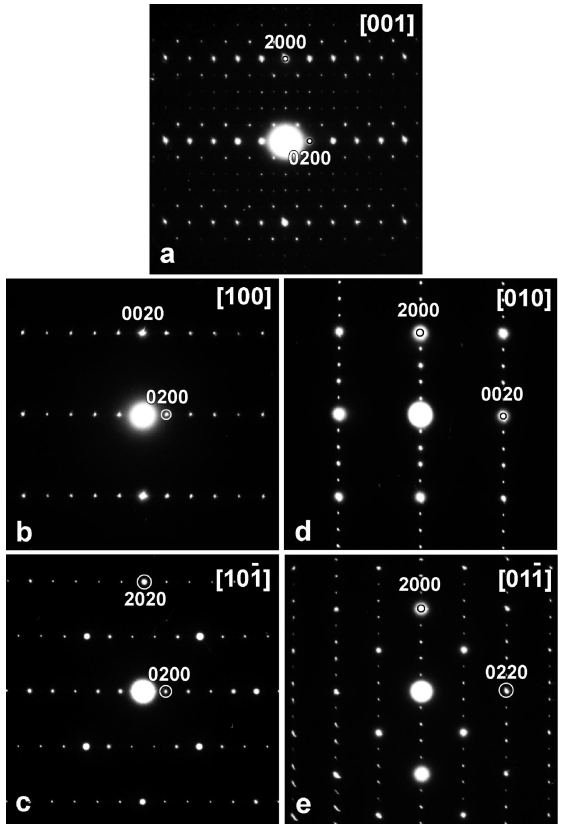

Figure 4. ED patterns of the $x = 0.4$ compound.

solutions can be written as $Ba_4In_{4+4\alpha}Mg_{2-4\alpha}O_{12+2\alpha}$ ($0.4 \leq \alpha \leq 0.5$). However, it should be noted that in every sample, some crystallites were occasionally found where the α value deviates from that dictated by the chemical composition. This can be attributed to local Mg inhomogeneities.

The ED patterns of $Ba_4In_{5.6}Mg_{0.4}O_{12.8}$ are shown in Figure 4. Similar to the ED patterns of the $x = 0$ material, the set of subcell reflections is clearly identified; it can also be indexed on a face-centered orthorhombic lattice with a_0, b_0, c_0. According to $\alpha = 2/5$, the second-order satellites are located at commensurate positions along **a*** dividing the 2000 reciprocal lattice vector into five equal parts inducing an $a = 5a_0$ superstructure. The spots with $0kl0$, k, l = odd are absent on the [100] ED pattern of the $x = 0.4$ phase because of the significantly increased splitting of the satellites, which moves them away from the [100] reciprocal lattice plane.

The observed reflection conditions $hklm$: $h + k + m = 2n$, $h + l = 2n$, $k + l + m = 2n$; $h0lm$: $m = 2n$ correspond to the superspace groups $Xmmm(\alpha00)0s0$ or $Xmm2(\alpha00)0s0$ with centering vectors (0, 1/2,1/2,1/2), (1/2,0, 1/2,0), (1/2,1/2,0,1/2). According to the acentric structures of $Ba_4In_6O_{13}$[15] and $Sr_4Fe_6O_{13}$,[19] we have adopted the acentric superspace group $Xmm2(\alpha00)0s0$ (in a primitive basis $Fmm2(\alpha10)0s0$ with a modulation vector $\mathbf{q} = \alpha\mathbf{a}_0^* + \mathbf{b}_0^*$). Pérez et al reported a solution of the incommensurately modulated $Sr_4Fe_6O_{13-\delta}$ crystal structure in the superspace group $X'maa(\alpha00)$ (a subgroup of $Xmmm(\alpha00)0s0$), where X' stands for the (0,1/2,1/2,1/2) centering vector (the *acb* setting is chosen by Pérez et al, but all further considerations are performed in the *abc* setting).[8] It should be noted that the $hklm$: $h + l + m = 2n$, $h0lm$: $h = 2n$, $hk0m$: $h = 2n$ reflection conditions of this superspace group allow the $h0lm$: h = even, l, m = odd reflections to have nonzero intensities. However, on the experimental ED patterns of the $Ba_4In_{6-x}Mg_xO_{13-x/2}$ solid solutions such reflections are systematically extinct (see the [010] ED patterns in Figures 2e and 4d). The $X'maa(\alpha00)$ superspace group also underestimates the symmetry of the average structure. According to this group, the average unit cell should be *A*-centered, thus imposing no restrictions on the h index of the $hkl0$: h, $l \neq 0$ reflections. However, the $hkl0$: k, $l \neq 0$ reflections with $h + k$ = odd and $h + l$ = odd are clearly absent on the [01$\bar{1}$] ED pattern of the $x = 0.4$ compound (Figure 4e). This allows us to exclude the $X'maa(\alpha00)$ superspace group for the $Ba_4In_{6-x}Mg_xO_{13-x/2}$ solid solutions.

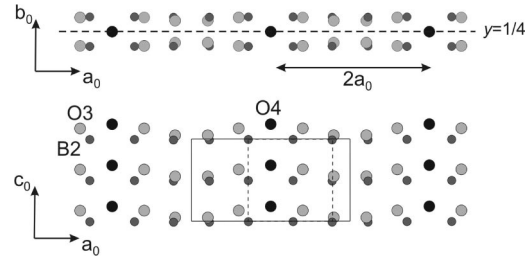

Figure 5. Structure of the $B_2O_{2.5}$ layer in $A_4B_6O_{13}$. The B2, O3, and O4 atoms are marked as small dark grey circles, large grey, and large black circles, respectively. The unit cell of $A_4B_6O_{13}$ with $2a_0$, b_0, c_0 is outlined with a solid line. The dashed line shows the unit cell of the average structure with a_0, b_0, c_0.

3.3. Superspace Model. Because single crystals of the $Ba_4In_{6-x}Mg_xO_{13-x/2}$ compounds are not available, we performed the structure refinement from X-ray powder diffraction data. Because of the inherent limitations of powder diffraction techniques, the number of refineable parameters in the superspace model should be reasonably constrained.[20] To construct the superspace model, the $A_4B_6O_{13}$ (A = Sr, Ba, B = Fe, Co, In) crystal structure will be considered in detail.[15,19,21] The average structure with $a_0 \approx a_p\sqrt{2}$, $b_0 \approx 20.5$Å, $c_0 \approx a_p\sqrt{2}$, $Fmm2$ space group, and $A_4B_6O_{12+2\alpha}$ composition can be represented as a sequence of layers $-AO-BO_2-AO-B_2O_{2+\alpha}-AO-BO_2-AO$, alternating along the b axis. According to the building principles of the $Sr_4Fe_6O_{12+2\alpha}$ compounds,[5–8] the modulations are confined to the $B_2O_{2+\alpha}$ layers. In the average structure these layers consist of B2 and O3 atoms arranged according to the NaCl-type structure and extra rows of O4 oxygen atoms resulting in a $B_2O_{2+\alpha}$ composition of the layer and a $A_4B_6O_{12+2\alpha}$ formula. In the $B_2O_{2.5}$ layers of the $A_4B_6O_{13}$ structure ($\alpha = 1/2$), the extra oxygen rows are parallel to the c axis and located at $y = 1/4$ (Figure 5); the extra oxygen rows appear every $2a_0$. In the average structure the O4 atoms are located at the idealized 1/4,1/4,z, $z \approx 1/4$ position. The occupancy modulation for this position is described with a steplike occupational modulation function (crenel function), which

(19) Yoshiasa, A.; Ueno, K.; Kanamaru, F.; Horiuchi, H. *Mater. Res. Bull.* **1986**, *21*, 175–181.

(20) Dusek, M.; Petricek, V.; Wunschel, M.; Dinnebier, R. E.; van Smaalen, S. *J. Appl. Cryst.* **2001**, *34*, 398–404.

(21) Fjellvåg, H.; Hauback, B.C.; Bredesen, R. *J. Mater. Chem.* **1997**, *7*, 2415–2419.

is defined by the width of the step Δ in x_4 and its midpoint x_4^0 so that atoms within the Δ interval have an occupancy factor equal to 1, otherwise the occupancy factor is equal to zero.[22,23] Applying the *Fmm*2 space group, there are four O4 atoms per one $A_4B_6O_{12+2\alpha}$ formula unit that requires $\Delta(O4) = \alpha/2$ with $x_4^0(O4) = 1/4$, as fixed by symmetry.

The rows of the O4 atoms separate the $B_2O_{2+\alpha}$ layer into blocks consisting of B2 and O3 atoms. In every block in $Ba_4In_6O_{13}$, the In2 and O3 atoms are displaced along the *a* axis away from the O4 atoms towards the center of the blocks as one can see on the [001] projection of the $B_2O_{2+\alpha}$ layer (Figure 5).[15] The whole block then becomes compressed along *a*. The displacement of the O3 atoms is much more pronounced than that for the B2 atoms and can be described with the sawtooth function $\mathbf{u} = 2\mathbf{u}_0[(x_4 - x_4^0)/\Delta]$, $x_4^0 - \Delta/2 < x_4 < x_4^0 + \Delta/2$, where $\mathbf{u}_0$ is the maximal displacement amplitude expressed by its components ($u_{0,x}$, $u_{0,y}$, $u_{0,z}$) along the x_1, x_2, x_3 axes, x_4^0 and Δ having the same meaning as for the steplike occupational modulation function.[24] The x_4^0 for the O3 atom is fixed by symmetry to either $x_4^0 = 1/4$ or $x_4^0 = 3/4$. Because the maximal displacement occurs near the O4 rows, the x_4^0 for the O3 atoms should be shifted by 1/2 with respect to $x_4^0(O4) = 1/4$, so that $x_4^0(O3) = 3/4$ should be chosen. The O3 atoms should retain full occupancy corresponding to $\Delta(O3) = 1$. The displacements of the B2 and O3 atoms along the *b* and *c* axes cannot be modeled with the sawtooth function because of their antisymmetric behavior that will lead to a splitting of these atomic positions in the 3D structure. They have to be described by a combination of harmonic functions which should be symmetric with respect to $x_4 = 1/4, 3/4$.

This setup of occupational domains and atomic displacements is directly related to the polyhedral representation of the structure of the $B_2O_{2+\alpha}$ layers (more general description of this approach is given in ref [16]). Together with the O2 atoms from the neighboring AO layers, the O3 and O4 atoms form a 5-fold coordination environment of the B2 cations. The BO_5 polyhedra adopt an irregular shape intermediate between trigonal bipyramid and tetragonal pyramid. In the $A_4B_6O_{13}$ crystal structure one can select chains of edge-sharing BO_5 polyhedra, running along the *c* axis. These chains are combined into double polyhedral bands by edge sharing through the rows of O4 atoms. Because of a strong deviation of the shape of these BO_5 polyhedra from perfect trigonal bipyramidal or tetragonal pyramidal, the assignment of a certain geometry is to some degree subjective. Yoshiasa et al considered these polyhedra to be more close to tetragonal pyramids in the $Sr_4Fe_6O_{13}$ structure.[19] Recently, Pérez et al have reconsidered this interpretation proposing that the shape of the FeO_5 polyhedra in these bands is more close to trigonal bipyramid in the anion-deficient $Sr_4Fe_6O_{13-\delta}$ structure.[8] Between these bands, other double bands of BO_5 polyhedra are located. These BO_5 polyhedra were described as either trigonal bipyramids (Yoshiasa et al.[19]) or tetragonal pyramids (Pérez et al.[8]). Yoshiasa et al.[15] discussed both types of polyhedra in the $Ba_4In_6O_{13}$ structure as strongly distorted tetragonal pyramids. As will be shown further by the results of the Rietveld refinement of the $x = 0$ and $x = 0.4$ structures, the notations proposed by Pérez et al seem to describe more correctly the geometry of the BO_5 polyhedra, and we will adopt them for further discussions. The occurrence of the double bands of the trigonal bipyramids (TB_2) is related to the density of the O4 rows and, hence, to the α value. Assuming now that the trigonal bipyramidal bands are always double bands, the thickness of the tetragonal pyramidal (TP) bands should be variable. The ratio between the amount of B-cations in the trigonal bipyramidal and the tetragonal pyramidal coordination is $\alpha/(1 - \alpha)$. Representing α as a rational number i/j, there will be i TB_2 bands per one $B_2O_{2+\alpha}$ layer in the supercell with $a = ja_0$. Then the average thickness of the TP bands (counted as the number of BO_5 polyhedra in the band along the *a* axis) is expressed as $2(j - i)/i = 2(1 - \alpha)/\alpha$. To keep a uniform sequence of TP bands, p bands of $\{2(1 - \alpha)/\alpha\}$ thickness should alternate with $(1 - p)$ bands of $(\{2(1 - \alpha)/\alpha\} + 1)$ thickness ($\{2(1 - \alpha)/\alpha\}$ denotes the integer part of $2(1 - \alpha)/\alpha$). The relative amount of the TP bands with different thicknesses can be calculated from the equation

$$2(1-\alpha)/\alpha = p\{2(1-\alpha)/\alpha\} + (1-p)(\{2(1-\alpha)/\alpha\} + 1)$$

Thus the polyhedral sequence in the $B_2O_{2+\alpha}$ layers can be directly inferred from the α value. For the $Ba_4In_{6-x}Mg_xO_{13-x/2}$ compounds α varies between 1/2 and 2/5. In this α region, only double TP_2 and triple TP_3 bands are present with a relative amount of the TP_2 bands $p = 5 - 2/\alpha$. One can see that the TB_2 bands alternate only with the TP_2 bands for $\alpha = 1/2$ and only with the TP_3 bands for $\alpha = 2/5$. Such limiting cases and the intermediate $\alpha = 4/9$ case are shown in Figure 6. When the α value is less than 2/5, TP bands with a thickness of four BO_5 polyhedra should appear. One quadruple TP_4 band then alternates with one TB_2 band for $\alpha =$

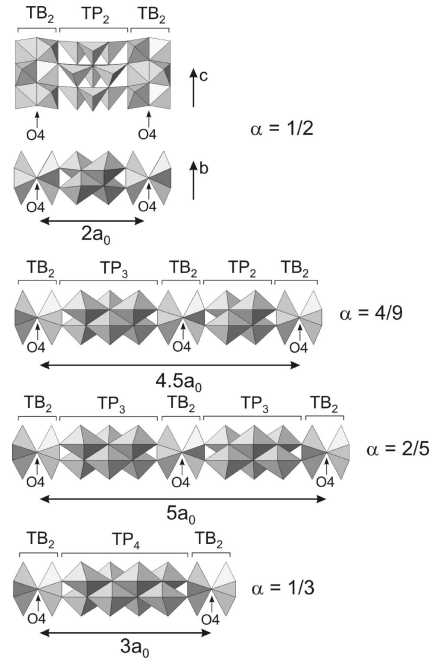

Figure 6. Arrangement of the TB and TP bands in the $B_2O_{2+\alpha}$ layers for different α values.

(22) Van der Lee, A.; Evain, M.; Monconduit, L.; Brec, R.; Rouxel, J.; Petricek, V. *Acta Crystallogr., Sect. B* **1994**, *50*, 119–128.
(23) Petricek, V.; van der Lee, A.; Evain, M. *Acta Crystallogr., Sect. A* **1995**, *51*, 529–535.
(24) Petricek, V.; Gao, Y.; Lee, P.; Coppens, P. *Phys. Rev. B* **1990**, *42*, 387–392.

1/3 (Figure 6). This was observed in the $Fe_2(Bi_{0.69}Sr_{2.31})Fe_2O_{9.5-1/2\delta}$ crystal structure.[9] Possible 3D space groups for commensurately modulated $A_4B_6O_{12+2\alpha}$ compounds derived from the *Xmm*2(α00)0*s*0 superspace group for rational α components of the modulation vector and some particular and general values of the initial modulation "phase" *t* are given in ref 6.

3.4. Rietveld Refinement. The derived superspace model was used to refine the crystal structures of the $x = 0$ and $x = 0.4$ compositions of the $Ba_4In_{6-x}Mg_xO_{13-x/2}$ solid solution. The satellites up to second order were taken into account. The refined α value for the $x = 0$ structure is 0.49506(6), in good agreement with the ED data. In the $x = 0$ structure, the atomic displacements for the Ba1, In1, In2, O1, and O2 atoms were described by a Fourier series:[20,25]

$$U_\lambda(\bar{x}_4) = \sum_n A_{n,\lambda}\sin(2n\pi\bar{x}_4) + B_{n,\lambda}\cos(2n\pi\bar{x}_4)$$

where $U_\lambda(\bar{x}_4)$ is the displacement along the λ coordinate and *n* is the order of the Fourier expansion. The determination of the coefficients of the harmonic position modulation functions from X-ray powder diffraction data is not a straightforward procedure. Because of the low intensity of the satellite reflections (the relative intensity of the most intense satellites does not exceed 5%) and their overlap with the reflections of the average structure, a calculation of a reliable Fourier map is not possible. The signs and values of the coefficients of the position modulation functions were determined using a trial-and-error procedure. The coefficients whose refined values were comparable with the standard deviations were then set to zero. This procedure revealed only a negligible position modulation for the equatorial oxygen atoms in the octahedral layer (O1 atom); it was not further included into the refinement. For the O3 atoms, the linear displacements along the *a* axis and the harmonic position modulation along the *c* axis were refined. The position modulations for the O4 atom were not refined. The *z* coordinates of the O2 (apical oxygen atom of the $In1O_6$ octahedra) and O3 atoms were very close to 0 and 1/2, respectively and demonstrated large standard deviations. The *z* coordinates for these atoms were fixed in further refinement cycles that did not influence the reliability factors but made the refinement more stable. At the final stage, the atomic coordinates and the coefficients of the position modulation functions were refined simultaneously. The thermal parameters for the oxygen atoms in the $x = 0$ structure had a tendency to become slightly negative. They were fixed to $U_{iso} = 0.01Å^2$ for the final refinement. The experimental, calculated, and difference powder XRD profiles for the $x = 0$ structure are shown in Figure 7. The crystallographic parameters are given in Tables 2 and 3. The main interatomic distances are listed in Table 4.

In the $x = 0.4$ structure, α does not deviate from the commensurate 2/5 value. This structure can be described in a 3D supercell with $a = 5a_0$, $b = b_0$, $c = c_0$, and *Bba*2 ($t = 0$) space group, as was proposed from HREM observations in ref 6. However, because of a huge amount of refineable parameters and the strong correlations between them in the 3D supercell, the refinement from powder XRD data was impossible. The structure was refined as a commensurate case corresponding to $t = 0$. The $Ba_2In_2O_5$ admixture phase (weight fraction of 7.3%) was also included into the refinement. To reveal the location of the Mg atoms, we refined the occupancy factors of In1 (octahedrally coordinated position) and In2 (the position in the $B_2O_{2+\alpha}$ layers with CN = 5). The g(In1) = 0.992(4) and g(In2) = 0.914(4) values were obtained. It reflects that In is substituted by Mg only in the In2 position. The estimated electron density at

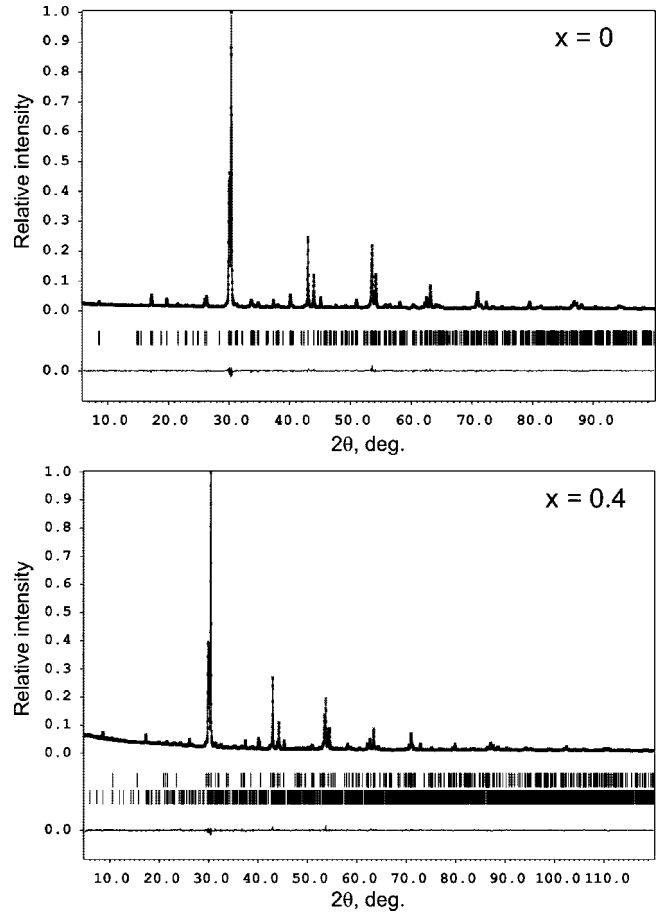

Figure 7. Experimental, calculated, and difference X-ray powder diffraction profiles for the $x = 0$ and $x = 0.4$ structures. The upper tick bar on the $x = 0.4$ profile marks the positions of the reflections from the $Ba_2In_2O_5$ admixture.

Table 2. Selected parameters from the Rietveld refinement for $Ba_4In_6O_{12.99}$ and $Ba_4In_{5.6}Mg_{0.4}O_{12.8}$

	$Ba_4In_6O_{12.99}$	$Ba_4In_{5.6}Mg_{0.4}O_{12.8}$
(3+1)D space group	X*mm*2(α00)0*s*0 x = (0, 1/2, 1/2, 1/2), (1/2, 0, 1/2, 0), (1/2, 1/2, 0, 1/2)	
a (Å)	5.94092(8)	5.92998(7)
b (Å)	20.5944(3)	20.4639(3)
c (Å)	5.96241(9)	5.97266(8)
q	0.49506(6)**a***	2/5**a***
cell volume (Å^3)	729.50(2)	724.78(2)
calcd density (g/cm^3)	6.581	6.444
2θ range, step (deg)	$6 \le 2\theta \le 100$, 0.02	$5 \le 2\theta \le 120$, 0.02
radiation, λ (Å)	1.5406	1.5406
R_I (all reflections)	0.040	0.062
R_I (main reflections)	0.026	0.048
R_I (1st order satellites)	0.051	0.071
R_I (2nd order satellites)	0.057	0.079
R_P, R_{wP}	0.042, 0.057	0.040, 0.055

(25) Van Smaalen, S. *Incommensurate Crystallography*; Oxford University Press: New York, 2007.

Table 3. Atomic Positions, Parameters of the Modulation Functions, And Thermal Parameters for $Ba_4In_6O_{12.99}$

atom	x_0	y_0	z_0	U_{iso} (Å^2)
Ba1	1/2	0.09050(8)	-0.010(2)	0.0218(5)
	$B_{1,x} = -0.0031(11)$, $A_{1,y} = 0.0012(2)$, $A_{1,z} = -0.012(1)$, $A_{2,x} = -0.011(2)$, $B_{2,z} = -0.0167(4)$			
In1	0	0	0	0.008(1)
	$A_{1,y} = 0.0111(3)$			
In2	0	0.2091(1)	−0.013(2)	0.0246(7)
	$B_{1,x} = -0.016(1)$, $A_{2,x} = 0.006(2)$, $B_{2,z} = -0.0843(4)$			
O1	0.263(7)	0	0.225(7)	0.01
O2	0	0.1146(5)	0	0.01
	$A_{1,z} = -0.043(6)$, $B_{2,z} = 0.015(3)$			
O3	0	0.2043(7)	1/2	0.01
	$u_{0,x} = -0.193(5)$, $u_{0,y} = u_{0,z} = 0$, $x_4{}^0 = 3/4$, $\Delta = 1$, $B_{2,z} = 0.055(2)$			
O4	1/4	1/4	0.320(8)	0.01
	$x_4{}^0 = 1/4$, $\Delta = \alpha/2 = 0.24753(3)$			

Table 4. Main Interatomic Distances for $Ba_4In_6O_{12.99}$ and $Ba_4In_{5.6}Mg_{0.4}O_{12.8}$ (Å)

	$Ba_4In_6O_{12.99}$			$Ba_4In_{5.6}Mg_{0.4}O_{12.8}$		
distance	min	max	avg	min	max	avg
Ba1−O1 ×2	2.62(3)	2.81(3)	2.73(3)	2.67(3)	2.83(3)	2.75(3)
Ba1−O1 ×2	2.82(3)	2.98(3)	2.90(3)	2.76(3)	2.96(3)	2.88(3)
Ba1−O2 ×2	2.95(1)	3.08(1)	3.017(8)	2.943(7)	3.061(5)	3.002(5)
Ba1−O2	2.76(2)	3.32(6)	3.00(3)	2.89(7)	3.04(6)	2.97(6)
Ba1−O2	2.71(6)	3.29(2)	3.05(3)	2.99(6)	3.16(7)	3.07(6)
Ba1−O3	2.39(1)	2.70(2)	2.50(2)	2.48(2)	2.80(4)	2.57(2)
In1−O1 ×2	2.06(4)	2.07(4)	2.06(4)	2.06(4)	2.06(3)	2.06(3)
In1−O1 ×2	2.16(4)	2.17(4)	2.17(4)	2.16(3)	2.16(3)	2.16(3)
In1−O2 ×2	2.17(1)	2.58(1)	2.37(1)	2.09(1)	2.51(1)	2.31(1)
In2−O2	1.95(1)	2.06(2)	2.01(1)	1.99(1)	2.03(2)	2.00(1)
In2−O3	1.94(3)	3.94(2)	2.78(2)	1.94(4)	4.02(2)	2.86(2)
In2−O3	1.94(3)	3.94(2)	2.87(2)	2.24(7)	3.38(5)	2.78(5)
In2−O3	1.83(2)	2.29(2)	2.02(2)	1.78(2)	2.33(4)	1.97(3)
In2−O3	2.02(3)	4.13(3)	2.96(2)	2.07(2)	4.49(4)	3.15(2)
In2−O3	2.21(3)	4.03(3)	3.13(2)	2.64(4)	4.15(7)	3.39(5)
In2−O4	1.94(2)	2.22(3)	2.08(3)	2.12(3)	2.12(3)	2.12(3)
In2−O4	1.94(2)	2.22(3)	2.08(3)	2.07(3)	2.07(3)	2.07(3)
In2−O4	2.33(4)	2.76(4)	2.54(4)	2.47(4)	2.47(4)	2.47(4)
In2−O4	2.33(4)	2.76(4)	2.54(4)	2.64(4)	2.64(4)	2.64(4)

this position corresponds to 0.9In + 0.1Mg, which is in perfect agreement with the $Ba_4In_{5.6}Mg_{0.4}O_{12.8}$ composition. Determination and refinement of the coefficients of the harmonic position modulation functions were performed in the same way as for the $x = 0$ structure. The oxygen atoms were refined with a common thermal parameter. The experimental, calculated, and difference powder XRD profiles for the $x = 0.4$ structure are shown in Fig. 7. The crystallographic parameters are given in Tables 2 and 5. The main interatomic distances are listed in Table 4.

3.5. HREM Observations. The refined crystal structures were confirmed by HREM observations. The [001] HREM image of the $x = 0$ structure at a focus of around -650Å is shown in Figure 8. From the comparison with the calculated [001] image, the darker layers correspond to the InO_2 octahedral layers. The rows of bright spots on both sides of these layers are the BaO layers sandwiching the $In_2O_{2+\alpha}$ layers. The bright dots correspond to projections of the cation columns. The modulation is seen as an alternation of darker and brighter areas along the $In_2O_{2+\alpha}$ layers; the darker areas correspond to the TB_2 bands, whereas the brighter areas correspond either to TP_2 or TP_3 bands. The TP_3 bands can be easily located by larger spacing between the dark areas.

Table 5. Atomic Positions, Parameters of the Modulation Functions, and Thermal Parameters for $Ba_4In_{5.6}Mg_{0.4}O_{12.8}$

atom	x	y	z	U_{iso} (Å^2)
Ba1	1/2	0.0910(1)	−0.017(1))	0.0249(6)
	$B_{1,x} = -0.0108(11)$, $A_{1,y} = 0.0054(3)$, $B_{2,y} = -0.0020(6)$, $B_{2,z} = -0.0106(8)$			
In1	0	0	0	0.013(1)
In2[a]	0	0.2092(2)	−0.037(1)	0.037(1)
	$B_{1,x} = -0.0211(10)$, $B_{2,z} = -0.0456(10)$, $B_{3,z} = 0.0531(8)$			
O1	0.275(5)	0	0.237(6)	0.023(4)
	$A_{1,y} = 0.0123(17)$			
O2	0	0.1123(6)	−0.026(9)	0.023(4)
	$B_{2,z} = -0.025(6)$			
O3	0	0.2071(9)	0.409(5)	0.023(4)
	$u_{0,x} = -0.239(8)$, $u_{0,y} = u_{0,z} = 0$, $x_4{}^0 = 3/4$, $\Delta = 1$, $B_{2,z} = 0.046(5)$			
O4	1/4	1/4	0.174(11)	0.023(4)
	$x_4{}^0 = 1/4$, $\Delta = \alpha/2 = 0.2$			

[a] Occupancy factor $g = 0.9In + 0.1Mg$.

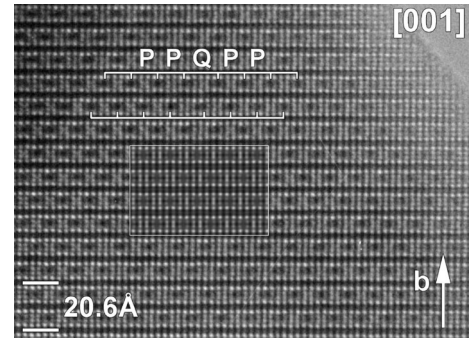

Figure 8. [001] HREM image of the $x = 0$ phase. A calculated image ($f = -650$ Å, $t = 60$ Å) is inserted. Sequence of separations between the centers of the TB_2 bands is marked with the brackets: separation P corresponds to the $TB_2-TP_2-TB_2$ sequence; separation Q corresponds to the $TB_2-TP_3-TB_2$ sequence.

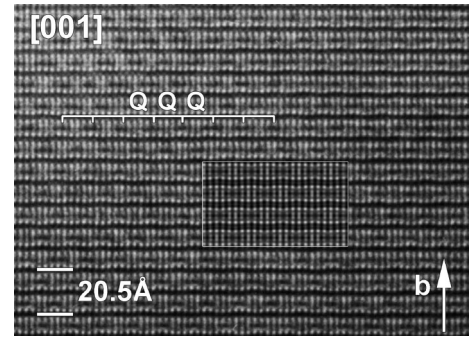

Figure 9. [001] HREM image of the $x = 0.4$ phase. A calculated image ($f = -650$ Å, $t = 30$ Å) is inserted. Sequence of separations between the centers of the TB_2 bands is marked with the brackets: separation Q corresponds to the $TB_2-TP_3-TB_2$ sequence.

A theoretical image was calculated using the structural data from the Rietveld refinement. The atomic positions of the modulated structures were transformed into a commensurate approximation with $a = 25a_0$, $b = b_0$, $c = c_0$ unit cell and $P1$ space group. A satisfactory agreement between the experimental and calculated ($f = -650$ Å, $t = 60$ Å) images was clearly obtained.

On the [001] HREM image of the $x = 0.4$ structure under the same focus conditions (Figure 9), the bright dots also correspond to projections of the cation columns. Again, the dark layers are the InO_2 layers and darker areas in the $In_2O_{2+\alpha}$

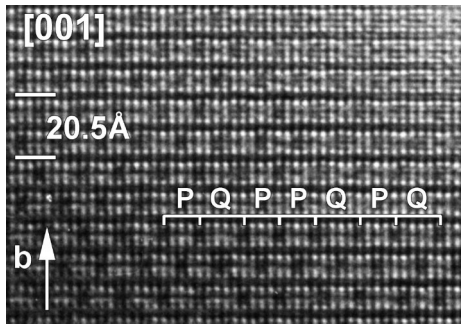

Figure 10. [001] HREM image of the $x = 0.2$ phase. Sequence of separations between the centers of the TB_2 bands is marked with the brackets: separation P corresponds to the $TB_2-TP_2-TB_2$ sequence; separation Q corresponds to the $TB_2-TP_3-TB_2$ sequence.

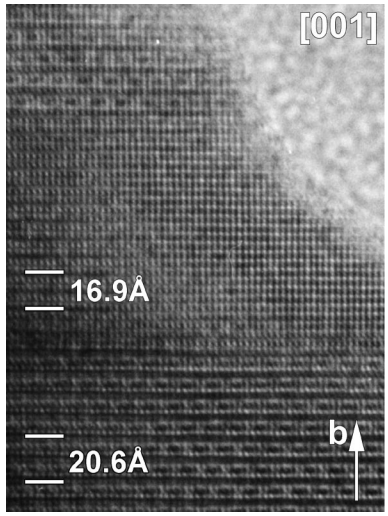

Figure 11. [001] HREM image of the $Ba_4In_6O_{13}$ sample demonstrating the presence of a $Ba_2In_2O_5$ brownmillerite slab.

layers mark the positions of the TB_2 bands. The distance between two successive TB_2 bands now corresponds exclusively to the TP_3 bands. To calculate the theoretical image, we used a commensurate 3D supercell with $a = 5a_0$, $b = b_0$, $c = c_0$ and *Bba*2 space group. The calculated and experimental images clearly match at $f = -650$ Å, $t = 30$ Å.

An intermediate case corresponding to $\alpha = 0.45$ is shown on the [001] HREM image of the $x = 0.2$ compound (Figure 10). For this composition, the TP_2 and TP_3 bands should be present in a ratio ~0.55:0.45. The occurrence of the TP_2 and TP_3 bands in nearly equal amounts is obvious from this HREM image; this proves that they uniformly alternate along the *a* axis.

The [001] HREM image of the $Ba_4In_6O_{13}$ sample (Figure 11) demonstrates a slab of the perovskite-type phase inside a matrix of the $x =$ phase. The repeat period of this phase along the normal to the intergrowth direction is equal to 8.45 Å, in agreement with the repeat period of the $Ba_2In_2O_5$ brownmillerite (16.74 Å[12]). It should be noted that a twice smaller periodicity should be observed for $Ba_2In_2O_5$ on the HREM image because of the *Icmm* space group. This observation confirms the suggestion that an appearance of the $BaIn_2O_4$ admixture can be partially caused by an occurrence of $Ba_2In_2O_5$ as an intergrowth inside the matrix of the main phase.

3.6. Electric Conductivity of $Ba_4In_{6-x}Mg_xO_{13-x/2}$. The typical Nyquist plots for Pt/$Ba_4In_6O_{13}$/Pt cell are shown in Figure 14. The equivalent circuit, fitting the whole frequency range of the EIS spectra, was chosen assuming that the materials exhibit both ionic σ_i and electronic σ_{el} types of conductivity, similar to that found for $Ba_2In_2O_5$[26] (see insert in Figure 14). Each element of the equivalent circuit corresponds to the physical process in the studied system: R_i (ionic resistance), R_{el} (electronic resistance), CPE_f (constant phase element), C_{dl} (electric double layer capacity), R_f (charge transfer resistance at the interface $Ba_4In_6O_{13}$/Pt/O_2), C_g (geometric capacity of the system). In our case, CPE_f (phase angle shift is about 45°) could be considered as a Warburg impedance, which is a result of the diffusion limitations at the $Ba_4In_6O_{13}$/Pt/O_2 interface. The data on σ_i and σ_{el} conductivities calculated from the EIS spectra using the equivalent circuit are only estimation; for the precise determination of these parameters additional experiments are required.

An accuracy of the equivalent circuit was verified on two $Ba_4In_6O_{13}$ samples with different thicknesses. The equivalent circuit parameters calculated from the EIS spectra are presented in Supplementary materials, Table 1. The conductivities were found to be almost congruent ($\sigma_{el} = 1.30 \times 10^{-4}$ Ohm^{-1} cm^{-1} and 1.33×10^{-4} Ohm^{-1} cm^{-1}, $\sigma_i = 1.43 \times 10^{-4}$ Ohm^{-1} cm^{-1} and 1.39×10^{-4} Ohm^{-1} cm^{-1}, respectively for the cylindrical samples with the thicknesses of 0.8 and 1.8 mm at $T = 650$°C, $p(O_2) = 0.21$ atm). The interface parameters (C_{dl}, CPE_f, and R_f) do not depend on the sample thickness, which confirms that the chosen equivalent circuit satisfies the conditions listed above.

Electric conductivity of $Ba_4In_6O_{13}$ was also studied under reduced oxygen partial pressure (Figure 15). Oxygen partial pressure reduction leads to considerable increase in electronic conductivity at the temperatures above 600 °C. Below 600 °C, conductivity does not depend on oxygen pressure. The precision of σ_i evaluation does not allow tracking $\sigma_i-P(O_2)$ dependence.

EIS measurements were also performed for the $Ba_4In_{6-x}Mg_xO_{13-x/2}$ solid solutions. The equivalent circuit parameters presented in the Supporting Information, Table 2, indicate that both ionic and electronic conductivity decrease with increasing Mg content in $Ba_4In_{6-x}Mg_xO_{13-x/2}$. The temperature dependence of conductivity for the $Ba_4In_{6-x}Mg_xO_{13-x/2}$ solid solutions is shown in Figure 16.

4. Discussion

The crystal structures of the $Ba_4In_{6-x}Mg_xO_{13-x/2}$ solid solutions are closely related to those of the $Sr_4Fe_6O_{13}$ compound and its anion-deficient derivatives. The modulations in the latter compounds are confined to the $Fe_2O_{2+\alpha}$ layer where the oxygen content is assumed to be directly related to the α component of the modulation vector. The $Ba_4In_{6-x}Mg_xO_{13-x/2}$ solid solutions undoubtedly establish the relationship between the α value and the oxygen content as $12+2\alpha$ according to the general formula of the solid solutions

(26) Goodenough, J.B.; Ruiz-Diaz, J.E.; Zhen, Y.S. *Solid State Ionics* **1990**, *44*, 21–31.

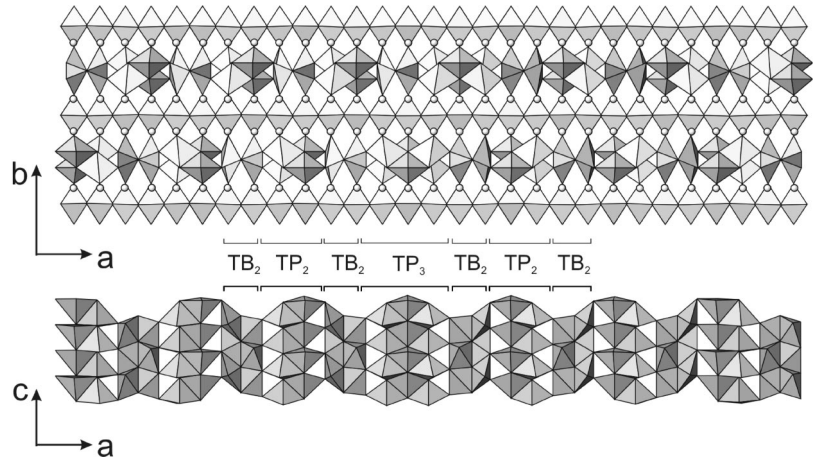

Figure 12. $Ba_4In_6O_{12.99}$ crystal structure. The In atoms are located in the shaded polyhedra, the Ba atoms are shown as spheres.

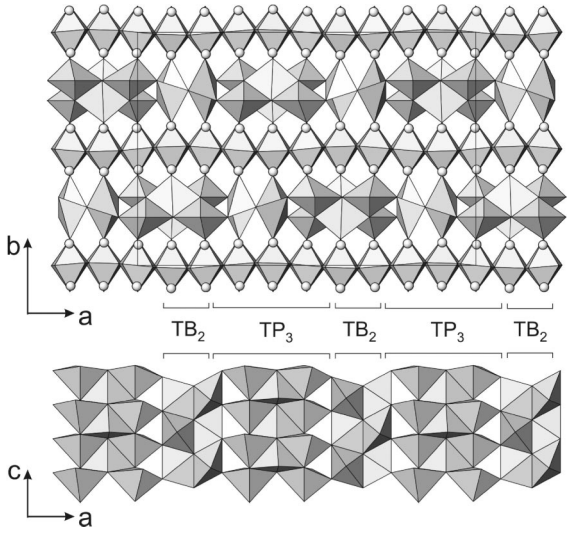

Figure 13. $Ba_4In_{5.6}Mg_{0.4}O_{12.8}$ crystal structure. The In, Mg atoms are located in the shaded polyhedra, the Ba atoms are shown as spheres.

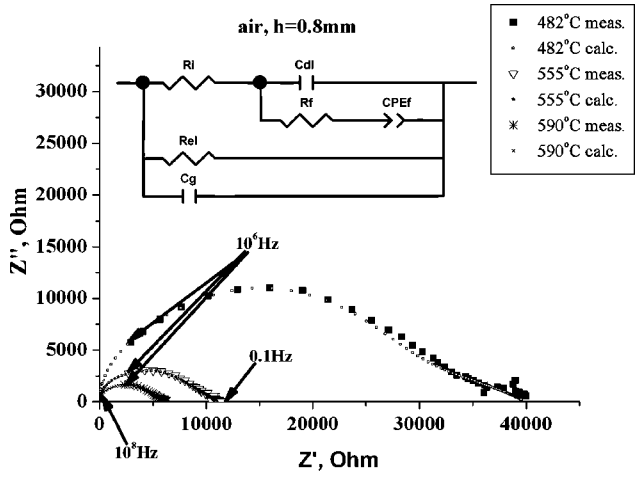

Figure 14. Nyquist plots for $Pt/Ba_4In_6O_{13}/Pt$ cell at low temperatures. The equivalent circuit for the EIS spectra of $Pt/Ba_4In_6O_{13}/Pt$ cells is shown as insert.

$Ba_4In_{4+4\alpha}Mg_{2-4\alpha}O_{12+2\alpha}$. In contrast to the Fe-based samples, where the oxygen content strongly depends on the synthesis conditions (temperature and partial oxygen pressure) because of the variable oxidation state of iron, in the $Ba_4In_{6-x}Mg_xO_{13-x/2}$ solid solutions, the oxygen content is

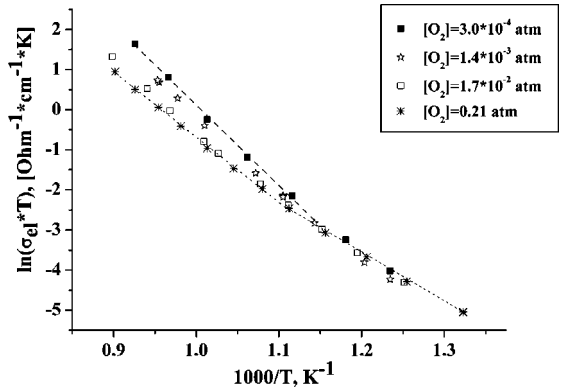

Figure 15. Arrhenius plot of electronic conductivity of $Ba_4In_6O_{13}$ under different oxygen partial pressures.

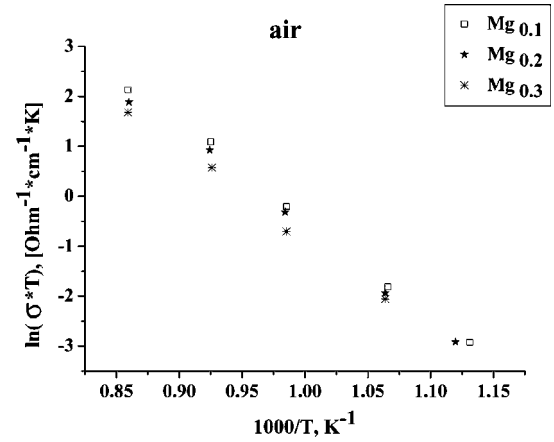

Figure 16. Arrhenius plot of conductivity of $Ba_4In_{6-x}Mg_xO_{13-x/2}$ with different Mg content.

predefined by the cation composition. The slight incommensurability of the $Ba_4In_6O_{13}$ compound has to be discussed in this light. The $\alpha = 0.49506(6)$ value implies a slight oxygen deficit for this compound corresponding to the $Ba_4In_6O_{12.99}$ composition. Such reasons as a minor amount of cation vacancies or small degree of replacement of In by a carbonate group can account for the oxygen depletion.

Because of the acentric superspace group, there is no split of atomic positions in the $B_2O_{2+\alpha}$ layers of the $Ba_4In_6O_{12.99}$ structure as it takes place in $Sr_4Fe_6O_{12.92}$,[8] but the atomic arrangement in these layers for both structures is similar.

Because the α value for $Ba_4In_6O_{12.99}$ is close, but not exactly equal to the commensurate value of 1/2, the TP_3 bands occur with rather low frequency in this structure (Figure 12), but their presence is undoubtedly proven by HREM. Only ~4% of all TP bands in this structure have the TP_3 configuration. In the $Ba_4In_{5.6}Mg_{0.4}O_{12.8}$ structure, only TP_3 and TB_2 bands are present (Figure 13). We avoid a detailed discussion of the variation of the atomic coordination of the In2 atoms along the $In_2O_{2+\alpha}$ layers because the structure information obtained from powder XRD data is not of ultimate precision. In both $Ba_4In_6O_{12.99}$ and $Ba_4In_{5.6}Mg_{0.4}O_{12.8}$ structures, the cations in the $B_2O_{2+\alpha}$ layers retain five-fold coordination, which deviates from both tetragonal pyramid and trigonal bipyramid, being, however, more close to tetragonal pyramidal in the TP bands and to trigonal bypiramidal in the TB bands. In most cases, the In2 atoms form three shorter (1.8−2.1 Å) and two longer (2.3−2.6 Å) bonds to the oxygen atoms. Using our data, we can not differentiate the TP_3 band from the MT−TP−MT band (MT, monocapped tetrahedron), as was observed in $Sr_4Fe_6O_{12.92}$.[8] No significant distortion was observed in the $In1O_2$ octahedral layers in $Ba_4In_6O_{12.99}$. However, these layers become noticeably undulated in the $Ba_4In_{5.6}Mg_{0.4}O_{12.8}$, which is related to a different thickness of the TP_3 and TB_2 bands along the *b* axis. The average in-plane In1−O distances and apical In1−O distances in the $In1O_6$ octahedra differ significantly (see Table 4), that was also observed in the $Ba_4In_6O_{13}$ crystal structure by Yoshiasa et. al.[15]

It should be noted that if the $B_2O_{2+\alpha}$ layer is represented as being composed of the BO_5 polyhedra and the coordination number of the B-cations does not vary, variation of the oxygen content is adopted because of the changing connectivity scheme of the BO_5 polyhedra. Within the TP and TB bands, the BO_5 polyhedra are linked through common edges (in the TP bands, partially by common corners), but the connection between the TP and TB bands is realized exclusively through corner-sharing. Increasing thickness of the TP bands with decreasing α results in a decrease of relative amount of connections through corner-sharing and, hence, in decreasing oxygen content.

The ionic radii of the Mg^{2+} and In^{3+} cations are close and their formal charges differ only by 1. From this point of view it would be difficult to expect any ordering of these cations. However, Mg^{2+} replaces In^{3+} only in the five-fold coordinated In2 position, but not in the octahedral In1 position. Possibly, the location of the cation with smaller charge in the edge-sharing $In2O_5$ polyhedra decreases the electrostatic repulsion between closely spaced cations thus providing the necessary energy gain for such partial ordering.

In the whole measured temperature range, $Ba_4In_6O_{13}$ behaves as a mixed electronic and ionic conductor with nearly equal values of σ_{el} and σ_i. The ionic and electronic conductivities of $Ba_4In_6O_{13}$ at 650 °C in air are comparable to those of $Ba_2In_2O_5$ ($\sigma_{el} \approx 3.50 \times 10^{-4}$ Ohm^{-1} cm^{-1}, $\sigma_i \approx 0.50 \times 10^{-4}$ Ohm^{-1} cm^{-1} at $T = 650$°C, $P(O_2) = 0.21$ atm[26,27]). The electronic conductivity of $Ba_4In_6O_{13}$ demonstrates significantly different behavior upon variation of $P(O_2)$ being compared to that of $Ba_2In_2O_5$. Increasing σ_{el} with increasing $P(O_2)$ in the 1×10^{-4} to 1 atm $P(O_2)$ range reflects that the *p*-type conductivity prevails for $Ba_2In_2O_5$.[26,27] Below 600 °C, where σ_{el} does not depend on $P(O_2)$, the charge carriers in $Ba_4In_6O_{13}$ are thermally activated electrons and holes. Above 600 °C, $Ba_4In_6O_{13}$ demonstrates decreasing σ_{el} with increasing $P(O_2)$ within a similar $P(O_2)$ range, which suggests electrons as main charge carriers responsible for σ_{el}. This difference can be qualitatively analyzed using a defect model proposed in.[27] In both $Ba_4In_6O_{13}$ and $Ba_2In_2O_5$ structures the octahedral perovskite layer is present where oxygen vacancies $V_O^{\bullet\bullet}$ can be easily created at low $P(O_2)$ that raises the electron concentration according to the reaction:

$$O_O \rightleftarrows 1/2O_2 + V_O^{\bullet\bullet} + 2e' \quad (1)$$

Frenkel-type O_i'' defects can be considered as responsible for creating holes at moderate $P(O_2)$

$$1/2O_2 + V_i \rightleftarrows O_i'' + 2h^{\cdot} \quad (2)$$

$Ba_4In_6O_{13}$ and $Ba_2In_2O_5$ differ significantly by the structure of the In−O block between the perovskite octahedral layers. In the brownmillerite structure of $Ba_2In_2O_5$, half of the octahedral InO_2 layers are transformed into the tetrahedral InO□ (□, oxygen vacancy) layers, where the Frenkel-type O_i'' defects are very favorable. The tendency of $Ba_2In_2O_5$ to generate holes at moderated oxygen pressures is thus confined to the presence of anion-deficient oxygen-vacancy ordered InO□ layers. In contrast to that, the NaCl-like $In_2O_{2+\alpha}$ layers in $Ba_4In_6O_{13}$ do not contain oxygen vacancies, which can act as V_i sites accepting oxygen atoms because of the increase of coordination number of the In^{3+} cations. Instead of that, oxygen nonstoichiometry in these layers is realized because of the changing connectivity scheme of the InO_5 polyhedra without variation of the coordination number of the In^{3+} cations that does not favor reaction 2. Thus electrons dominate as charge carriers in $Ba_4In_6O_{13}$ due to the reaction 1. Replacement of In^{3+} by Mg^{2+} decreases the conductivity because the Mg^{2+} cations can act as trapping centers for anion vacancies and Mg^{2+} are much less susceptible to the reduction than In^{3+}, which decreases the electron concentration.

5. Conclusion

By structural analysis of the $Ba_4In_{6-x}Mg_xO_{13-x/2}$ solid solutions, we prove that modulations in the $A_4B_6O_{12+2\alpha}$ materials arise from variable oxygen content and confirm the dependence of the length of the modulation vector on the oxygen content. The structural mechanism proposed for the $Sr_4Fe_6O_{12+2\alpha}$ phase is equally applicable to the $Ba_4In_{6-x}Mg_xO_{13-x/2}$ solid solutions with the only difference that in the latter the oxygen non-stoichiometry is caused by heterovalent cation replacement and not related to a variable oxidation state of the B-cations. A possibility of extending the family of these modulated structures towards compounds with excess oxygen was expected earlier related to the insertion of a single polyhedral band between the adjacent TP_2 bands.[6,8] The oxidized $Sr_4Fe_6O_{12+2\alpha}$ phases with the oxygen content corresponding to $\alpha > 0.5$ were reported (α

(27) Zhang, G.B. Smyth D.M. *Solid State Ionics* **1995**, *82*, 161–172.

$= 0.57$[28] and $\alpha = 0.7$[29]). One can expect that a broader range of oxygen content can be achieved using heterovalent cation replacement in $Ba_4In_6O_{13}$ at ambient oxygen pressure. Such solid solutions can be potentially interesting objects for discovering structural models of oxygen nonstoichiometry in this family of compounds.

Acknowledgment. This work was partially supported by the Russian Foundation of Basic Research (RFBR Grants 07-03-00664-a, 06-03-90168-a, and 05-03-34812-MIF-a). The authors are grateful to Dr. V. Petricek for valuable comments on Rietveld refinement.

Supporting Information Available: Crystallographic data in CIF format for $Ba_4In_6O_{12.99}$ and $Ba_4In_{5.6}Mg_{0.4}O_{12.8}$; tables of the equivalent circuit parameters calculated from the EIS spectra for the Pt/$Ba_4In_6O_{13}$/Pt and Pt/ $Ba_4In_{6-x}Mg_xO_{13-x/2}$/Pt samples (PDF). This material is available free of charge via the Internet at http://pubs.acs.org.

(28) Waerenborgh, J. C.; Avdeev, M.; Patrakeev, M. V.; Kharton, V. V.; Frade, J. R. *Mater. Lett.* **2003**, *57*, 3245–3250.
(29) Guggilla, S.; Armstrong, T.; Manthiram, A. *J. Solid State Chem.* **1999**, *145*, 260–266.

CM8004216